# Asymmetric Microelectrodes for Nanoliter Bubble Generation via Electrolysis

Eugene Yoon, *Member, IEEE*, and Ellis Meng, *Fellow, IEEE*

***Abstract*— Microfabricated devices for gas bubble generation via water electrolysis typically employ two electrodes of identical size (*i.e.* interdigitated electrodes or microelectrode pairs). Contrary to this practice, asymmetrically sized electrode pairs offer distinct advantages in the formation of single, trapped nanoliter-volume gas bubbles in microfluidic devices. Although such principles may apply generally to MEMS or micro-scale water electrolysis devices, our model system consisted of a Parylene C microfluidic structure to contain the bubble and embedded thin-film Pt electrodes immersed in 1× phosphate buffered saline solution. The geometric area of one microelectrode was constant (working electrode) while that of the second electrode (counter electrode) was varied over five orders of magnitude. Although increased counter electrode size increases overall device size, it provides improvements in various performance metrics. The largest tested counter electrode size resulted in 41% energy savings per bubble, improved bubble volume uniformity, enabled successful discrimination between $O_2$ versus $H_2$ gas generation, and achieved bubble stability exceeding 500 minutes (a 25× improvement over previous work). The underlying theory motivating the use of asymmetric electrodes is detailed and followed by experimental demonstration. Finally, a discussion on tradeoffs to assist in the design of MEMS-based electrolytic bubble generation devices is provided. [2021-0172]**

***Index Terms*— Microbubble, nanobubble, electrolysis, counter electrode, polarization, electrochemical, Parylene C.**

## I. Introduction

SINGLE gas bubbles generated via electrolysis in MEMS-based devices offer unique advantages for a variety of applications. Examples include the ability to generate bubbles on-demand and the potential to employ bubbles as sensing or actuating elements [1], [2]. Additionally, the need for cumbersome tubing to supply gas is obviated and moving parts are not required. These benefits have led to the development of several micromachined pumps [3], sensors [4], actuators [5] and other devices [6], [7] harnessing the utility of electrolytically generated micro- and nano-scale bubbles. They serve in use cases where miniaturization is critical such as implantable devices or cell-interfacing devices.

To generate bubbles via electrolysis, sufficient current or voltage must be applied between two electrodes immersed in aqueous solution [8]. Although several electrode pair configurations have been reported, MEMS-scale devices commonly employ two symmetric interdigitated electrodes (IDE) or two microelectrode pads of equal geometric surface area to achieve electrolysis (Table I). This approach emphasizes small device footprint but presents several electrochemically based drawbacks.

If electric pulses are applied on symmetric electrode pairs, both electrodes will polarize in equal and opposite directions. This phenomenon is directly responsible for several undesirable consequences. For instance, energy may be wasted per bubble generation event, the chemical composition of the gas may be difficult to control, and bubble dissolution behavior may be adversely affected. Therefore, this work investigates asymmetric electrode pairs in which the counter electrode is larger than the working electrode to constrain polarization to the working electrode only.

First, we address underlying theory governing the electrode size-dependence in the context of electrolytic bubble generation and then we describe experiments in which the counter electrode size is varied while holding the working electrode size constant. Analysis of the results is accompanied by a discussion of relevant scenarios where the benefits and disadvantages of asymmetric electrode sizing for bubble-based MEMS is well-suited.

## II. Theory

The impact of electrode size can be illustrated by using electrochemical potential diagrams (Fig. 1). Electrode polarization during application of a bubble-generating pulse can vary dramatically depending on the relative sizes of the two electrodes in use. The underlying reasons for this size-dependence are briefly explained herein and the reader is directed to references [8], [9] for additional background beyond the scope of this work.

### A. The Electrochemical Cell

An electrochemical cell contains an electrolyte solution and a minimum of two electrodes in contact with the solution. One electrode is often designated as the 'electrode of interest' and is termed the working electrode (WE). The second electrode

Manuscript received August 12, 2021; revised October 14, 2021; accepted November 1, 2021. Date of publication November 23, 2021; date of current version February 2, 2022. This work was supported in part by the U.S. National Science Foundation under Award EFRI-1332394, Award IIP-1601340, and Award IIP-1827773. Subject Editor K. Cheung. *(Corresponding author: Ellis Meng.)*

Eugene Yoon is with the Biomedical Engineering Department, University of Southern California, Los Angeles, CA 90089 USA (e-mail: eugenejy@usc.edu).

Ellis Meng is with the Department of Biomedical Engineering and the Department of Electrical and Computer Engineering, University of Southern California, Los Angeles, CA 90089 USA (e-mail: ellis.meng@usc.edu).

Color versions of one or more figures in this article are available at https://doi.org/10.1109/JMEMS.2021.3126789.

Digital Object Identifier 10.1109/JMEMS.2021.3126789

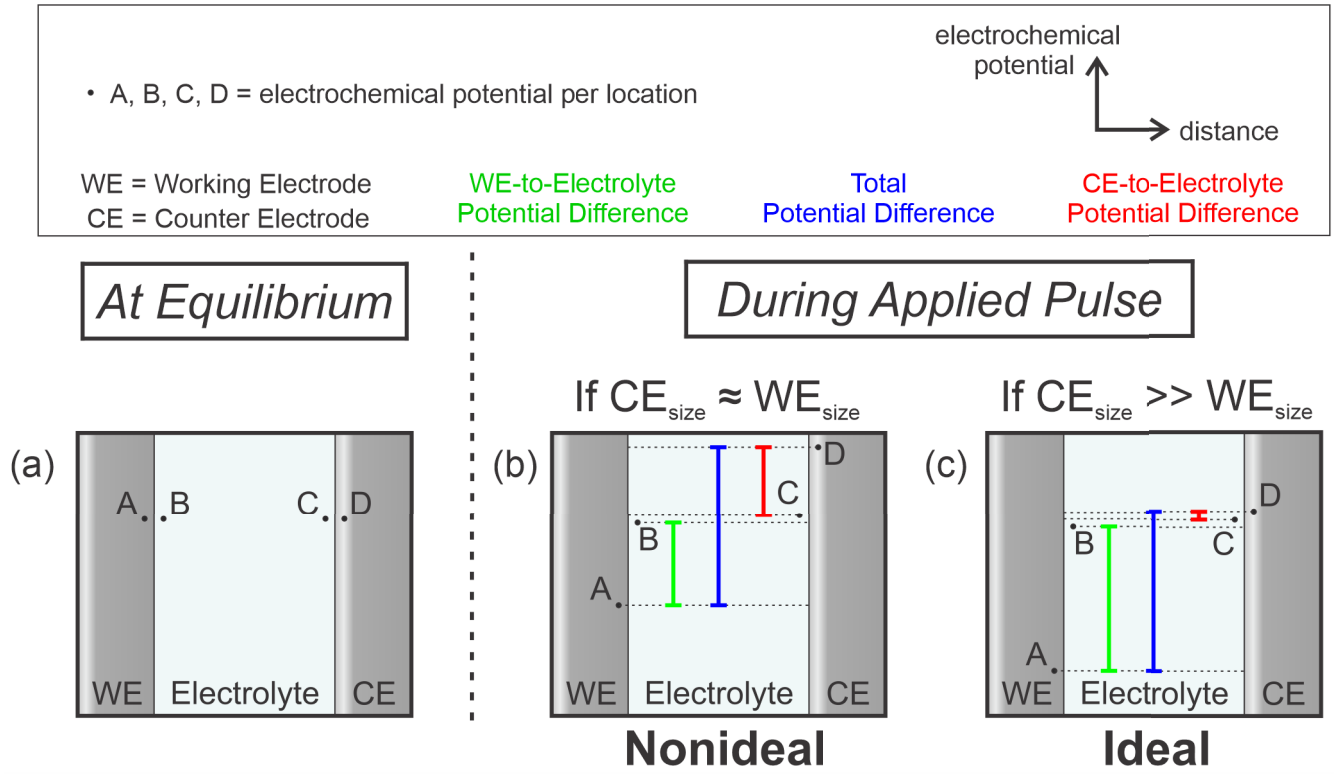


Fig. 1. Electrochemical potential diagrams to illustrate the effect of electrode pair sizing on polarization. (a) At equilibrium, all points along the electrochemical potential diagram are at approximately the same electrochemical potential. (b) If the electrodes are similarly sized (i.e., interdigitated electrodes or identical electrode pads) then polarization will occur in equal and opposite directions ($|E_{A-B}| = |E_{C-D}|$). (c) If the counter electrode is significantly larger than the working electrode, polarization will be predominantly localized to the electrode-to-electrolyte potential difference at the working electrode interface only ($|E_{A-B}| > |E_{C-D}|$).

TABLE I
ELECTRODE PAIR TYPE AND SPECIFIC APPLICATIONS OF MEMS-BASED DEVICES FOR ELECTROLYTICALLY GENERATED BUBBLES

| | | Electrode Pair Type | | |
|---|---|---|---|---|
| | | IDEs | Symmetric Pads | Other |
| Application Type | Micropump | [5], [18], [19], [20], [21], [3], [22], [23] | [24] | |
| | Sensor | [25], [26] | [2], [4], [17], [27], [28], [13], [29], [30] | |
| | Actuator | [18], [31] | [32], [33] | [34],[35] |
| | Other | [6], [7], [11], [36] | [37], [38], [39] | [40],[41] |

closes the circuit and is commonly referred to as the counter electrode (CE) although other nomenclature such as return, ground, and auxiliary electrode exist in the literature [8].

The two electrodes may be connected to the terminals of an applied voltage source which drives current flow between the WE and CE. This provides the driving force for redox reactions via electrochemical potential differences throughout the cell (Fig. 1). Although both voltage and electrochemical potential are often used interchangeably, their definitions are distinct. Voltage refers to the difference in electric potential between two points or with respect to Earth ground. Electrochemical potential ($E$) specifically refers to the combination of electrical and chemical potential (free energy). Like electric potential, electrochemical potential cannot be measured directly. Rather, electrochemical potential *differences* may be referenced to a dedicated reference electrode in 3-electrode cells, as is the case in this work. In other cases, the CE may serve as both a current sink and a pseudo-reference in 2-electrode cells. Earth ground is typically avoided as a reference because this may render measurements susceptible to ground loops or damage.

### B. Electrolysis

If the driving force is sufficiently large, electron transfer between the electrode and electrolyte may occur via faradaic reactions (*i. e.* electrolysis). We are primarily concerned with the water electrolysis reaction with the associated half-cell reactions in (1) and (2). By convention, half-cell reactions are written in the order of reduction.

If there is a sufficiently large potential difference during a pulse, reduction of the electrolyte may occur (1) at the cathode and (2) oxidation at the anode. The WE may serve as either the cathode or anode. Standard cell potentials in (1) and (2) are associated for each half-cell reaction, but they are

with respect to the standard hydrogen electrode (SHE) – a theoretical construct which is physically unattainable.

$$2H^+(aq) + 2e^- \rightarrow H_2(g), \quad E^\circ(V) = 0 \tag{1}$$

$$O_2(g) + 4H^+(aq) + 4e^- \rightarrow 2H_2O, \quad E^\circ(V) = 1.229 \tag{2}$$

It is possible convert standard cell potentials into values with respect to more practical reference electrodes such as the saturated calomel or Ag|AgCl electrode and to perform Nernst equation calculations that determine what potential differences are required to make electrolysis thermodynamically favorable. However, reaction kinetics, mass transfer considerations, double-layer capacitance, metal cleanliness, overpotentials, temperature, buffer strength, presence/absence of supporting electrolyte, and many other factors hinder accurate *a priori* prediction of electrolytic gassing potential difference values.

In practice, such information is typically obtained by empirically cycling the cell voltage between an upper and lower bound and measuring the resulting current via cyclic voltammetry (CV) [10]. The peaks and troughs of $i$-$E$ curves from CV effectively serve as 'electrochemical signatures' to denote the presence of half-cell reactions such as those for water electrolysis.

### C. The Electrode-to-Electrolyte Potential Difference

The fundamental driving force for electrochemical reactions is the electrode-to-electrolyte potential difference [9]. Note in Fig. 1 that the total applied potential difference, $E_{A-D}$ (blue), is the sum of the WE-to-electrolyte potential difference, $E_{A-B}$ (green), the CE-to-electrolyte potential difference, $E_{C-D}$ (red), and the potential drop across the electrolyte, $E_{B-C}$ (also called the $iR$ drop). A two-electrode system may only measure $E_{A-D}$ whereas the reference electrode in a three-electrode system may also enable approximate measurements of $E_{A-B}$ and $E_{C-D}$.

The relative contribution of each interfacial potential drop to the total applied potential depends strongly on the size of WE and CE. For systems with two equally sized electrodes, both will polarize in equal and opposite directions during an applied pulse (Fig. 1b). Conversely, for systems where the CE is much larger than the WE, polarization is predominantly restricted to the WE interface (Fig. 1c) since the CE's larger surface area imparts a larger double-layer capacitance. Electroneutrality dictates that the same amount of charge must pass through both the WE and CE. Therefore, mostly non-faradaic double-layer capacitive charging occurs at the CE, whereas electrode polarization induces faradaic reactions for gas evolution at the WE in Fig. 1c. Both cases in Fig. 1b and 1c experience the same total potential difference, but the specific apportionment of interfacial potential differences may have profound implications on control of electrolytic bubble generation.

### D. Implications on MEMS Electrolytic Bubble Devices

Gas evolution only requires one electrode-to-electrolyte potential difference to be large enough to drive a desired electrochemical reaction. Hence, polarization of both electrodes in scenarios such as Fig. 1b can result in wasted energy since only one interface actually needs to be polarized. Such power savings may be critical in applications that depend on battery life.

Other devices may heavily rely on the chemical composition of the generated gas such as $O_2$ generators for cell culture [11]. However, the hydrogen evolution reaction requires a smaller electrode-to-electrode potential difference than the oxygen evolution reaction for most aqueous systems at a neutral pH [8]. Therefore, $H_2$ gas will be preferentially generated if equally sized electrode pairs are employed because equal and opposite polarization will occur at both electrodes until one of them reaches the potential of $H_2$ evolution. By contrast, using a large and relatively non-polarizable CE allows effective control over the WE potential for selective $H_2$ (cathodic) or $O_2$ (anodic) gas evolution.

Because both gases have different solubilities in water ($4.5 \times 10^{-5}$ and $2.10 \times 10^{-5}$ cm$^2$/s at 25°C; $H_2$ and $O_2$, respectively [12]), using a large CE provides additional control over bubble dissolution behavior. Depending on the application, fast or slow dissolution may be desired. For instance, bubble-based pressure sensors experienced undesirably fast bubble dissolution ($<$ 20 minutes) [4] due to $H_2$ generation from equally sized electrode pairs.

## III. Design and Fabrication

### A. Design

We investigated the effect of CE size on single bubble generation with the device shown in Fig. 2. The design was adapted from previous work [13] and included a hollow microfluidic structure containing embedded electrodes. The device was constructed from thin-film platinum (Pt) sandwiched between two 10 $\mu$m layers of thin-film Parylene C (herein referred to as Parylene). The Pt was patterned into four 50 $\mu$m wide traces via standard photolithography techniques. These insulated traces emerged as exposed tips in the inner lumen of the Parylene microchannel as well as the hollow cavity at the microchannel's midpoint. The purpose of this cavity, or nucleation core, was to facilitate bubble nucleation and growth and subsequently allow the bubble to detach and reside in the microchannel. The distal ends of the microchannel had etched openings to allow electrolyte solution to enter and fill the microchannel.

### B. Fabrication

The main steps of the microfabrication process flow are illustrated in Fig. 3 and based on fabrication processes employed in past work [2], [13]. Briefly, 10 $\mu$m of Parylene was deposited on a silicon carrier wafer (PDS Labcoter 2010, Specialty Coating Systems, Indianapolis, IN). AZ 5214 photoresist (Integrated Micro Materials, Argyle, TX) was then spun on to define metal features in preparation for lift-off. An $O_2$ plasma descum (60 s, 100 W, 100 mtorr) was performed immediately prior to electron beam evaporation (CHA Mark 40, CHA Industries, Fremont, CA) of 200 nm of 99.99% Pt (PraxAir Inc., Danbury, CT). Special care was taken to prevent Pt cracking due to the thermal expansion mismatch

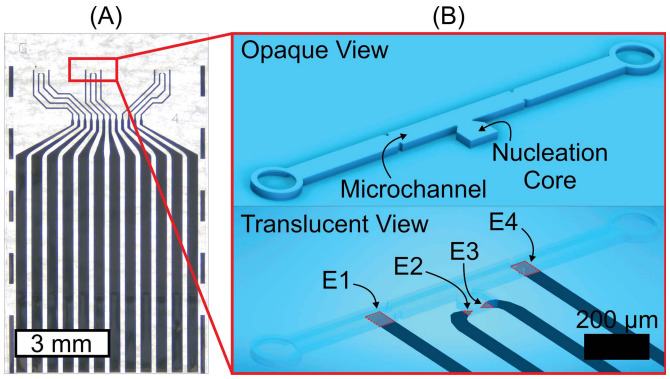


Fig. 2. Micrograph (a) and schematic illustrations (b) of device where Parylene (blue) is opaque or translucent in order to highlight hollow and/or embedded components.

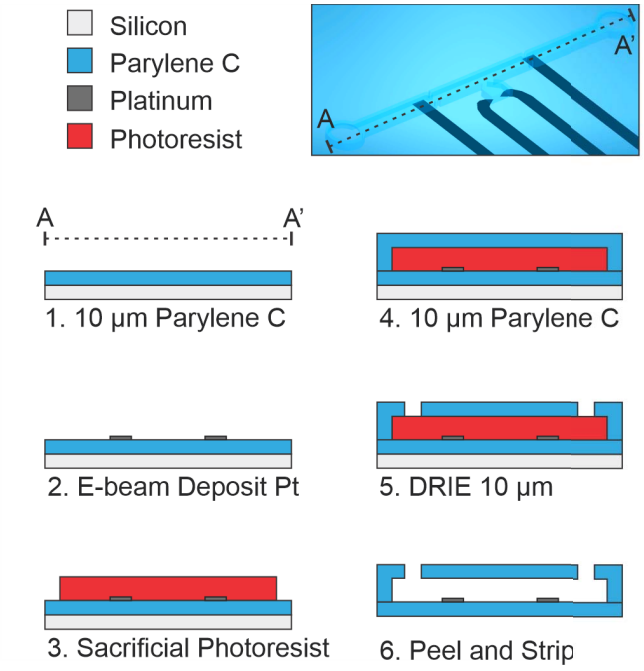


Fig. 3. Microfabrication process flow for the device under test. The A-A' cross section of interest runs along the longitudinal length of the device.

with Parylene. Without breaking vacuum, four depositions measuring 50 nm with 30-minute pauses in between each step were performed in a tool having a long throw distance (55 cm) [14]. Metal liftoff was achieved through 10-minute long sequential baths of acetone, isopropyl alcohol, and deionized water at room temperature.

Next, 16 $\mu$m of AZ P4620 (Integrated Micro Materials, Argyle, TX) was spun on to define the dimensions of the inner lumen of the microchannel and nucleation core by serving as sacrificial photoresist. Hard baking was intentionally omitted in order to prevent photoresist reflow which would alter the microchannel cross section. The same $O_2$ plasma descum was applied and 10 $\mu$m of additional Parylene was then deposited. Another 16 $\mu$m layer of AZ P4620 was spun on to serve as an etch mask in the ensuing deep reactive ion etch step. The mask selectively protected the wafer to define the perimeter of each testing die, distal openings of the microchannel, and device contact pads. At those regions, the top 10 $\mu$m of Parylene was removed by a modified Bosch process which alternated between fluoropolymer deposition ($C_4F_8$) and inductively coupled $O_2$ plasma etching [15] (Oxford Plasmalab 100, Oxford Plasma Technology, UK).

With the aid of a microscope, a razor blade was used to manually separate each die using the etched outline as a guide. Dies were then carefully peeled off the wafer with fine tweezers. Stripping of the sacrificial photoresist inside the hollow microfluidic structures required 2-hour long sequential baths of acetone, isopropyl alcohol, and deionized water with agitation due to diffusion-limited dissolution. After drying, devices were annealed for 48 hours at 200 °C in a vacuum oven (TVO-2, Cascade TEK, Irving, TX) which was purged 3× with $N_2$ gas [16]. Dies were mated at the contact pads with zero insertion force connectors (Hirose Electric Co., Ltd, Tokyo, Japan) which were soldered onto flat flexible cables for electrical access to downstream testing equipment. A polyethylene terephthalate backing provided the necessary thickness (~200 $\mu$m) for the connector to engage its closing latch.

## IV. Experimental Methods

### A. Image Processing

A compound microscope (PSM-1000, Motic, Hong Kong) with 200× magnification was used in conjunction with a mounted CMOS camera (PL-B776, Pixelink, Ottawa, Canada) for image capture at 10 fps. The image sampling rate necessitated use of custom Windows Management Instrumentation Command-line (WMIC) scripts to efficiently extract the file creation time with millisecond resolution.

Custom algorithms were built with the MATLAB Image Processing Toolbox (Mathworks, Natick, MA) to analyze bubble images and to extract the number of pixels corresponding to the bubble per image frame. The resolution was approximately 0.2 $\mu$m per pixel which corresponded to 0.00064 pL per pixel. A baseline image containing no bubble was subtracted from subsequent image frames containing bubbles. The resultant image was conditioned, binarized, and pixels corresponding to the bubble were counted in each frame (Fig. 4). The number of pixels was converted into $\mu m^2$ and multiplied by the sacrificial photoresist thickness which corresponded to the interior height of the microchannel (16 $\mu$m, as measured by profilometer) to arrive at an estimate for bubble volume. Special care was taken in the image conditioning step to partially count the shadow in the bubble boundary to account for the gas-liquid interface meniscus. The same algorithm was applied to all trials.

### B. Electrochemical Bubble Tests

In all experiments, dies containing 3 identical devices obtained from the same wafer were used to minimize processing variations. Experiments were conducted with devices mounted into the custom-machined testing fixture shown in Fig. 5. Dies were sandwiched between the bottom bulk acrylic and a 0.5 mm thick silicone gasket which was cut using a motorized vinyl cutter (Graphtec CE-6000, Graphtec America Inc., Irvine, CA). The gasket only covered a small horizontal

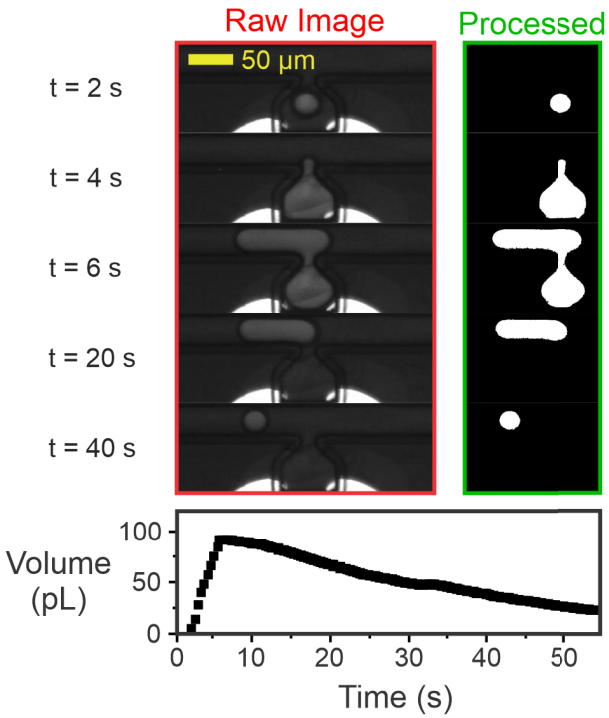


Fig. 4. Representative bubble growth trial. Images were capture at 10 fps and processed with a custom MATLAB algorithm to extract the bubble volume versus time.

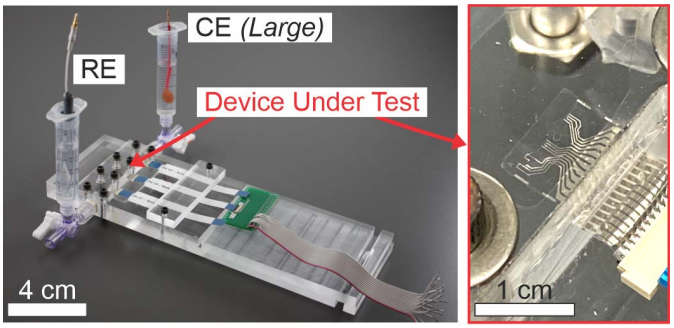


Fig. 5. Custom fixture used to conduct all experiments. Devices were submerged in 1× PBS inside a cavity defined by the silicone gasket and acrylic components of the fixture.

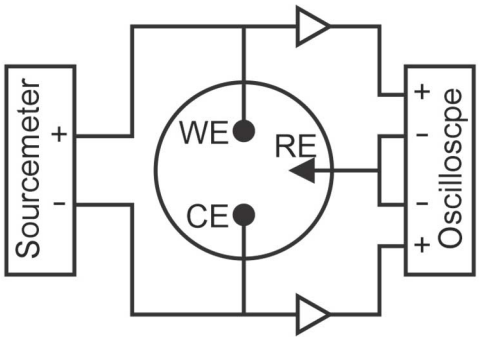


Fig. 6. Electrochemical circuit diagram to illustrate connection schemes between electrodes of interest and equipment.

TABLE II
SIZE DESIGNATIONS OF TESTED COUNTER ELECTRODES

| Name | Area ($\mu m^2$) | CE:WE Ratio |
|---|---|---|
| Small | $2.3 \times 10^2$ | 1:1 |
| Medium | $2.5 \times 10^3$ | 10:1 |
| Large | $1.6 \times 10^7$ | 70,000:1 |

segment across the die to create a watertight seal while the actual test structures resided in the gasket's opening. We defined this space as the testing chamber. A laser cutter (Epilog, Golden, CO) was used to fabricate an acrylic cover piece which was placed on top of the gasket. Screws were used to apply pressure on the gasket to prevent potential leaks in the testing chamber.

Holes bored into the bottom acrylic block were fitted with luer connectors to allow 1× PBS to enter the testing chamber via stopcocks and syringe tubes. The syringe tubes provided convenient access to the testing chamber for the Ag|AgCl (3M KCl) reference electrode (RE) (BASi®, West Lafayette, IN) and a macro scale counter electrode constructed from Pt wire (1 cm long, 0.5 mm Ø) and potted with epoxy (Epotek 353ND-T, Epoxy Technology Inc., Billerica, MA). A PCB breakout board was used to electrically access individual device electrodes. Experiments were conducted at room temperature and atmospheric pressure. Parafilm sheets (not shown) were used to cover syringe tube openings in between experiment trials to account for potential changes in conductivity due to evaporation. The initial total 10 mL of 1× PBS did not significantly decrease (<1% volume) throughout the duration of experiments. The working electrode (WE) was designated as E2 in Fig. 2. To test 3 different CE sizes, the small, medium, and large CE were designated as E3, E4, or the macro-scale Pt wire; respectively. Table II displays the relevant sizing parameters of the electrodes.

Prior to any experimentation, a Gamry Reference 600 potentiostat (Gamry Instruments, Warminster, PA, USA) was used to conduct electrochemical impedance spectroscopy to characterize WE properties (3 electrode cell; room temperature; 1× PBS; 10 MHz to 1 Hz; 25 mV signal; no DC bias; Faraday cage). Afterwards, experiments were conducted with a custom electrochemical setup while being viewed under a compound microscope (3-electrode cell; room temperature; 1× PBS; no Faraday cage). As illustrated in Fig. 6, the current was controlled while simultaneously measuring the potential (or vice versa) between the WE-CE via a sourcemeter unit (Keithley 2400). A 2-channel oscilloscope (Tektronix, Beaverton, OR) allowed for simultaneous measurement of the WE-RE and CE-RE potential difference which served as a proxy for the respective electrode-to-electrolyte potential differences. Voltage buffering was required to prevent unwanted current shunting and accomplished by high input impedance (1 TΩ) op-amps (TLC2274ACN, Texas Instruments, Dallas, TX) where the output was connected to its inverting input and the signal source was connected to the non-inverting input.

An experiment similar to cyclic voltammetry was conducted to monitor the amount of unwanted polarization of the CE during gas evolution. Using a custom LabVIEW program, the WE-CE potential was set to start at 0 V and decrease at a sweep rate of −100 mV/s. The potential was allowed

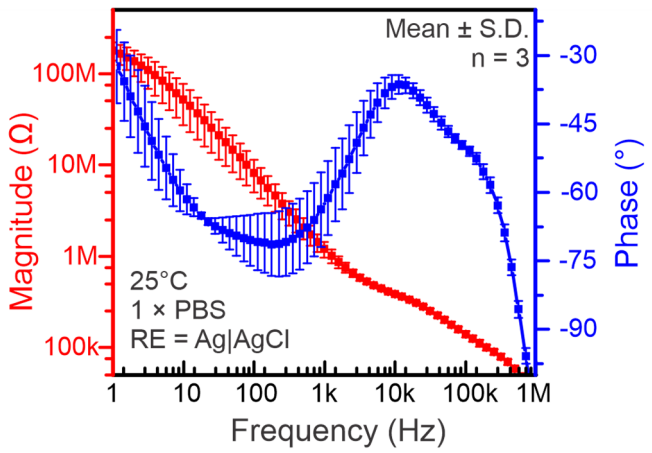


Fig. 7. Electrochemical impedance spectroscopy of the working electrode (E2 of Fig. 2) on each of the 3 identical devices under test prior to any testing.

to decrease until the onset of gas generation due to the hydrogen evolution reaction (HER) could be observed in real-time. As soon as bubble generation was observed, the sweep rate was changed to +100 mV/s. The WE-CE potential then increased until the onset of the oxygen evolution reaction (OER) could be observed. At that moment, the sweep rate was changed to -100 mV/s again and the experiment terminated when the WE-CE potential returned to 0 V. Three trials per device per CE size were conducted. The measured variables of interest were the WE-RE potential and CE-RE potential.

Afterwards, the same 3 devices were subject to cathodic pulses (−0.6 $\mu$A, 6 s). Each device underwent 3 sets of testing in total, where each set was designed to explore each CE size. A testing set consisted of 8 pulses where each pulse was separated by approximately 2 hours. Testing order across devices and CE sizes was scrambled to control for the rate of non-negligible polymer insulation degradation due to prolonged soaking in electrolyte solution. The measured variables of interest were the WE-CE, WE-RE, and CE-RE potential as well as the bubble volume. More specifically, the variance in bubble volume per set was recorded and calculated into pooled standard deviations.

Lastly, 8 anodic and 8 cathodic pulses (±0.6 $\mu$A, 6 s) were applied in random order with a new but identical device. Only the large Pt wire CE was used in this experiment to ensure proper polarization of the WE. The measured variables of interest in this experiment were identical to those of the previous experiment.

## V. Results

### A. Electrochemical Impedance Spectroscopy (EIS)

EIS was used to characterize the working electrodes (E2 of Fig. 2) from three identical devices which had been co-fabricated on the same die. The resulting impedance magnitude and phase are plotted in Fig. 7 with error bars denoting standard deviation. Low inter-device variability was observed, indicating successful device fabrication, and establishing comparable electrochemical starting points for ensuing experiments.

### B. Voltage Sweeping to Determine Gassing Limits With Respect to Counter Electrode Size

Electrode polarization with respect to CE size was qualitatively investigated by sweeping WE-to-CE potential at ±100 mV/s between gassing limits. The WE-to-RE and CE-to-RE potential was simultaneously measured. This experiment was repeatably conducted for 3 different CE sizes and representative results are displayed in Fig. 8.

For all CE sizes, the WE-RE potential difference approached approximately −1.4 V for the onset of $H_2$ gas evolution and +2.0 V for $O_2$ gas evolution. The CE-RE potential difference displayed similar behavior, if inverted, for the small CE case. Notably, in the large CE case, the CE-RE potential difference remained relatively unchanged from its starting value. The medium CE case demonstrated behavior intermediate to the small and large case. Since the WE-CE potential difference is essentially the sum of the WE-RE and CE-RE potential difference, Fig. 8 illustrated that use of larger CE will confine the majority of the potential drop to the WE-to-electrolyte interface for all applied potential difference values. Conversely, small CE usage revealed unwanted sharing of the potential drop across both the WE and CE interfacial potential differences. Additionally, data exhibited more noise for smaller CE sizes.

### C. Cathodic Pulses Versus Counter Electrode Size

As shown in Fig. 9a, pulses of −0.6 $\mu$A and 6 seconds were applied for different CE sizes. These parameters consistently generated bubbles. Potential differences were measured throughout the pulse duration and revealed that usage of large CE effectively prevented CE polarization. If a large CE was employed, the WE-CE and WE-RE potential differences were almost identical, indicating that the majority of the potential drop was localized to the WE-to-electrolyte interface.

The energy consumed to generate each bubble was computed by multiplying the average WE-CE potential drop during a pulse, the current amplitude, and pulse duration. Results are displayed in Fig. 9c and illustrated that small CE usage required more energy than that of large CE. The former caused both WE and CE to polarize until one of the electrode-to-electrolyte potential differences was sufficient to drive electrolysis. A significant amount of energy is therefore wasted in polarizing both electrodes. Conversely, a properly designed cell with a large CE effectively prevented CE polarization and confined the potential drop to the WE interface. In this experiment, there was a 41% difference in energy savings when comparing the small (12.0 $\mu$J) and large (7.1 $\mu$J) case.

Image processing tools extracted the bubble volume in each trial which allowed for computation of the pooled standard deviation among different CE size datasets. Theoretically, the equivalent amount of charge injected in each trial should yield equivalent bubble volumes, but the measured average values were 0.11, 0.16, and 0.11 nL for the small, medium, and large; respectively. Pooled standard deviations across datasets (32.7, 29.4, and 19.8 pL for small, medium, and large cases; respectively) revealed that larger CE experiments yielded slightly more uniform bubble volumes.

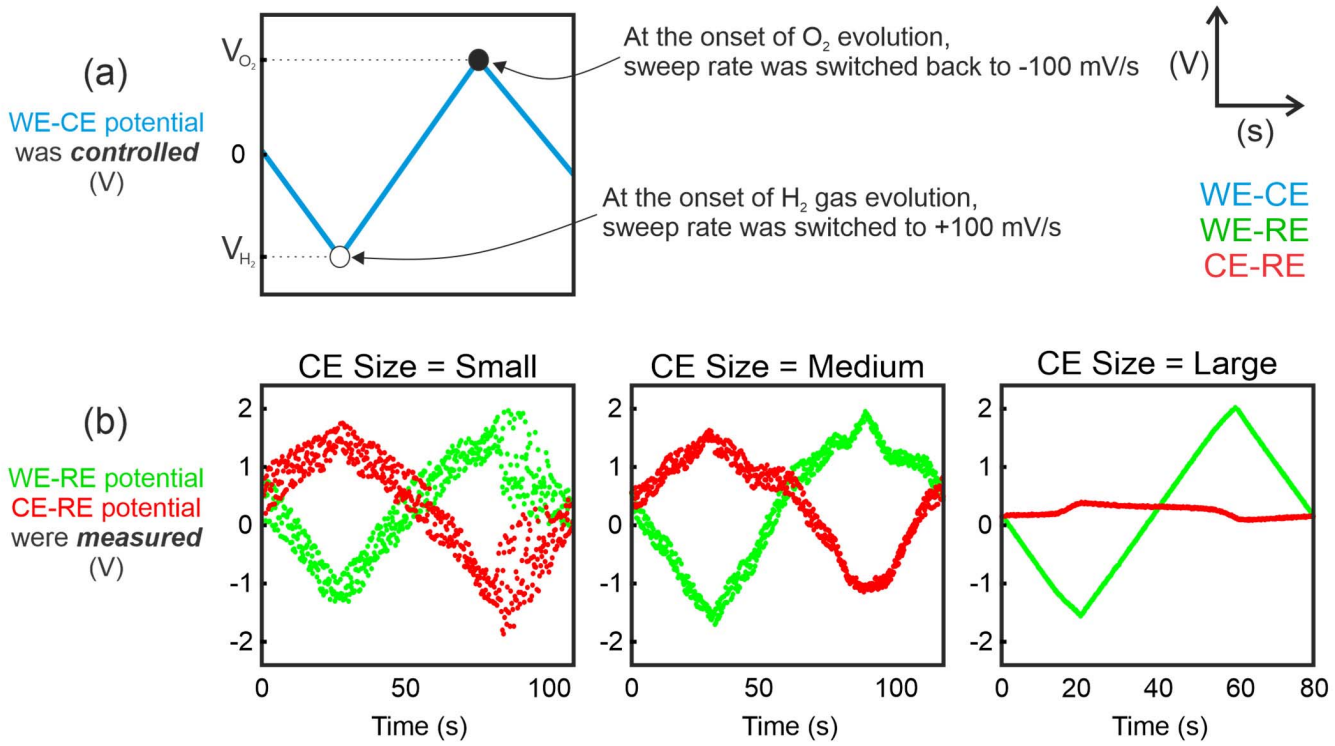


Fig. 8. Representative voltage sweeping results to determine gassing limits as a function of counter electrode size. (a) The total electrochemical cell potential difference was swept at ±100 mV/second while simultaneously observing gas evolution in real-time. (b) The electrode-to-electrode potential for both the working electrode and counter electrode is plotted for instances where the counter electrode size was allowed to vary.

### *D. Cathodic vs. Anodic Pulses With Large Counter*

When a large CE was employed to effectively restrict polarization to the WE interface, the use of positive versus negative current revealed clear differences. Fig. 10 displays the bubble volume versus time at the onset of the pulse (6 s duration, ±0.6 $\mu$A). Notably, the negative applied current generated approximately double the amount of gas (0.13 nL) as the positive current (0.07 nL). The total amount of time required for bubbles to dissolve (Fig. 11) revealed that bubble lifetime was notably longer for bubbles generated with positive rather than negative current (36 ± 6.1 min versus 10.3 ± 0.7 min; respectively; mean ± standard deviation; n = 8 each). Notably, the bubbles from positive current had longer lifetimes despite their smaller starting volumes (Fig. 10). The +0.6 $\mu$A and 6 s pulse generated bubbles only filled up approximately one third of the total microchannel length, so a test bubble with +0.6 $\mu$A and 18 s was generated to fill the entire channel. The bubble lifetime was 500 minutes (data not shown).

## VI. Discussion

One major benefit of large CE use in MEMS-based electrolytic bubble devices is the energy savings of each bubble generation (up to 41%; from 12.0 $\mu$J to 7.1 $\mu$J). In certain sensors designed for implantation, such savings may significantly extend battery life because electrolytic generation consumes orders of magnitude more energy than other operations such as sensing or data transfer [4], [17].

Additionally, bubbles generated via large CE may be more uniform in volume. Electrode surface inhomogeneities and uncleanliness are known to affect electrochemical reaction repeatability. Larger CEs were hypothesized to reduce such effects as the relative ratio of contaminated versus nominal area may be more favorable than that of smaller CEs. Uniform bubble generation is required for accurate measurements in devices using the bubble as a sensing element. Our experiments demonstrated a correlation between improved bubble uniformity for larger CE, but Parylene delamination may have been responsible for weakening the statistical significance.

Prolonged immersion of Parylene in PBS is known to cause water and ion permeation [14] which may accelerate Parylene-Pt delamination. Additionally, pulsing at high charge densities most likely exacerbated delamination. Such effects engender more contact between electrolyte and metal, increasing double layer capacitance such that less charge is spent in gas-evolving faradaic reactions. Hence, special care was taken to account for the duration of Parylene soaking by scrambling the testing order on devices and CE sizes. However, our throughput was limited because our imaging equipment could only test one device at a time. More throughput and data are anticipated to improve the statistical significance.

Large CE use enables control over gas chemical composition and consequently control over bubble lifetime due to each gas's characteristic water solubility. Results in Fig. 10 and Fig. 11 illustrated this principle through the adherence to stoichiometric expectations dictated by half-cell reactions. Twice the amount of $H_2$ gas was generated in the reduction reaction as $O_2$ in the oxidation reaction. Although less $O_2$ was generated, $O_2$ bubbles had longer lifetimes as expected by its lower solubility.

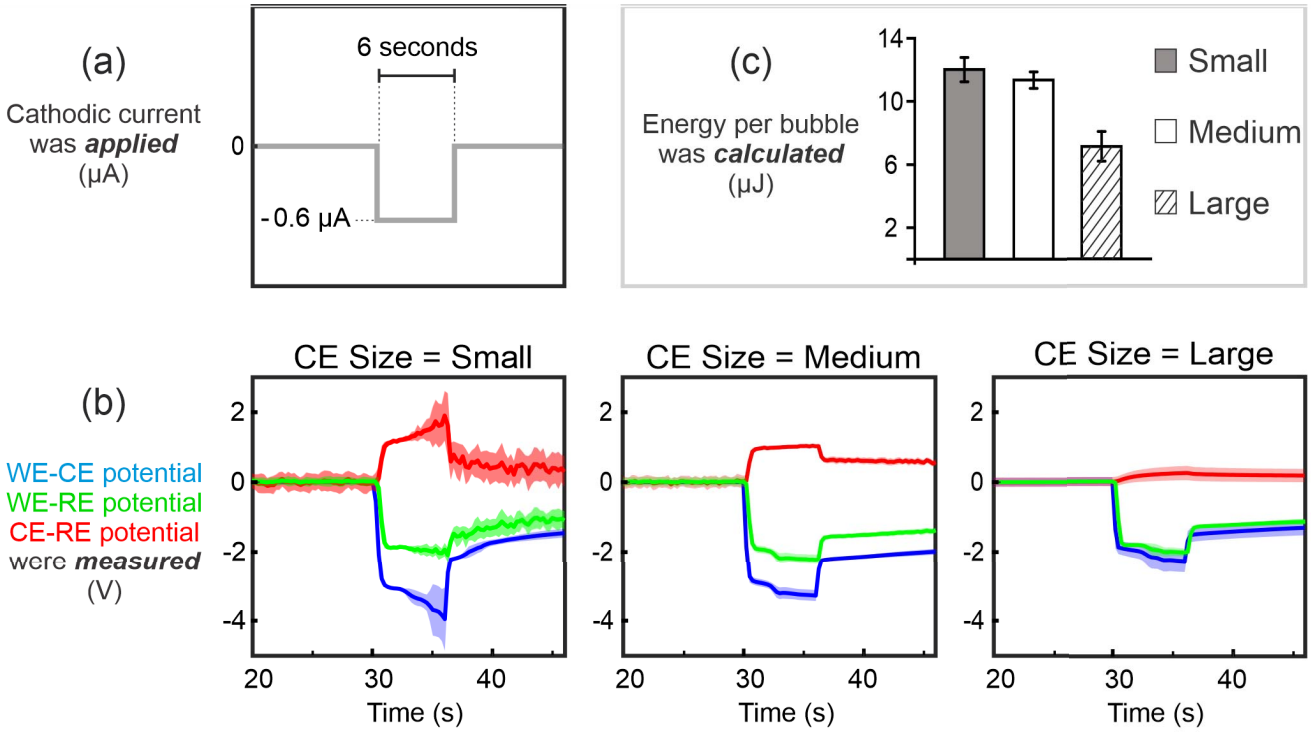


Fig. 9. (a) Cathodic pulses (−0.6 $\mu$A for 6 seconds) were applied to generate bubbles, (b) the various potential differences normalized to their starting values were measured as a function of CE size (n = 8 pulses per CE size dataset; shaded regions denote standard deviation), and (c) multiplying the average total WE-CE potential difference per pulse by the current amplitude and duration allowed for computation of the average energy required per bubble.

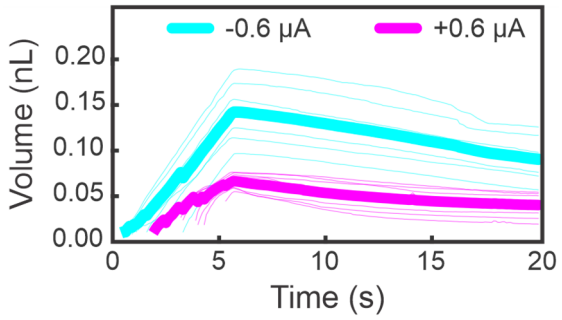


Fig. 10. Bubble volume (nL) versus time for experiments using a large counter electrode with positively or negatively applied current pulse. Thick lines represent averaged data and thin lines represent individual trials.

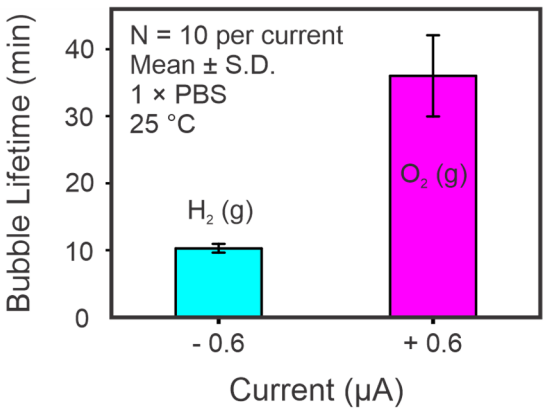


Fig. 11. The amount of time required for generated bubbles to completely dissolve (i.e., bubble lifetime) significantly varied by the usage of positive or negative applied current (36 ± 6.1 min versus 10.3 ± 0.7 min; respectively; mean ± standard deviation) when a large CE was used.

Devices employing the electrolytic bubbles as the sensing element may benefit greatly from such control over dissolution behavior. For instance, the bubble with a 500 minute lifetime represented a 25× improvement over previous work [4], [17]. Premature gas recombination may have been accelerated in MEMS-based electrolytic bubble devices featuring IDEs or equally sized electrode pads due to the close proximity of both electrodes. As both become polarized and produce redox species for their respective half-cell reactions, such species may diffuse across relatively short distances to effectively hasten the recombination reaction at the opposite electrode site. Close placement of electrode pairs is often accompanied by the justification of increased electrolytic efficiency since the *iR* drop is directly related to the inter-electrode distance. However, the *iR* drop is typically 1 or 2 orders of magnitude smaller than interfacial potential drops [9].

The greatest advantage of equally sized and closely spaced electrode pairs (and conversely the greatest drawback in the use of large CE) for MEMS-based electrolytic single bubble devices may be the device footprint. Larger CE will increase device size which may prove unacceptable for certain applications. In this work, the microfabricated medium CE size was selected to investigate a 10:1 ratio between CE:WE, but the Pt wire for the large CE demonstrated most effectiveness with a 70,000:1 ratio. Although such macroscale and non-micromachined components may be difficult to incorporate into MEMS-based device design, very large microfabricated pads may be designed to serve as counters

to achieve the same benefits. Alternatively, if hermetic metal casings are intended for use with the device, they may serve as the large counter electrode as is common in cardiac pacemakers.

## VII. Conclusion

Electrolytic generation of a single nanoliter scale bubble in a chamber via MEMS-based devices was investigated with particular focus on the effect of the size of the counter electrode. Experiments were conducted to illustrate the extent of electrode polarization on the working and counter electrode-to-electrolyte interface. Use of a CE whose surface area was several orders of magnitude greater than the WE demonstrated that polarization was mostly confined to the WE interface during electrolytic bubble generation. Conversely, usage of equally sized WE and CE showed equal and opposite polarization.

The polarization apportionment throughout the electrochemical circuit displayed significant implications on device performance. Localized control of polarization through the use of the large CE showed 41% reduction in energy consumption per bubble, improved bubble volume uniformity, successful discrimination between $O_2$ versus $H_2$ generation, and 500-minute bubble lifetime (a 25$\times$ improvement over previous work). The main tradeoff against these advantages may be the increased device footprint associated with a larger electrode. However, it may be possible to obtain large counter electrode benefits without directly fabricating one if the electrochemical circuit is closed by metal hermetic casing instead. The theory and results presented here guide future device design involving electrolytically generated single bubbles.

## Acknowledgment

The authors would like to thank Alfonso Jimenez for microfabrication assistance, Dr. Alex Baldwin and Dr. Dan Merrill for insightful discussions, and the members of the USC Biomedical Microsystems Laboratory for their assistance.

## References

[1] J. D. Suter, C. J. Hohimer, J. M. Fricke, J. Christ, H. Kim, and A. T. Evans, "Principles of meniscus-based MEMS gas or liquid pressure sensors," *J. Microelectromech. Syst.*, vol. 22, no. 3, pp. 670–677, Jun. 2013.

[2] L. Yu, C. A. Gutierrez, and E. Meng, "An electrochemical microbubble-based MEMS pressure sensor," *J. Microelectromech. Syst.*, vol. 25, no. 1, pp. 144–152, Feb. 2016.

[3] I. V. Uvarov, S. S. Lemekhov, A. E. Melenev, and V. B. Svetovoy, "Exploding microbubbles driving a simple electrochemical micropump," *J. Micromech. Microeng.*, vol. 27, no. 10, Oct. 2017, Art. no. 105009, doi: 10.1088/1361-6439/aa8914.

[4] C. A. Gutierrez and E. Meng, "A subnanowatt microbubble pressure sensor based on electrochemical transduction in a flexible all-parylene package," in *Proc. IEEE 24th Int. Conf. Micro Electro Mech. Syst.*, Jan. 2011, pp. 549–552.

[5] R. Sheybani, H. Gensler, and E. Meng, "A MEMS electrochemical bellows actuator for fluid metering applications," *Biomed Microdevices*, vol. 15, no. 1, pp. 37–48, Feb. 2013.

[6] P.-H. Kuo *et al.*, "A remotely controlled locomotive IC driven by electrolytic bubbles and wireless powering," in *IEEE Int. Solid-State Circuits Conf. (ISSCC) Dig. Tech. Papers*, Feb. 2014, pp. 322–324.

[7] S. W. Lee, O. C. Jeong, and S. S. Yang, "The fabrication of a micro injector actuated by boiling and/or electrolysis," in *Proc. IEEE 11st Annu. Int. Workshop Micro Electro Mech. Syst. Invest. Micro Struct., Sensors, Actuat., Mach. Syst. (MEMS)*, 1998, pp. 51–56.

[8] A. Bard and L. Faulker, "Introduction and overview of electrode processes," in *Electrochemical Methods: Fundamentals and Applications*, 2nd, ed. Hoboken, NJ, USA: Wiley, 2000, pp. 1–43.

[9] D. R. Merrill, "The electrode—Materials and configurations," in *Essential Neuromodulation*, 1st, ed. New York, NY, USA: Academic, 2011, pp. 107–152.

[10] D. W. Kumsa, N. Bhadra, E. M. Hudak, S. C. Kelley, D. F. Untereker, and J. T. Mortimer, "Electron transfer processes occurring on platinum neural stimulating electrodes: A tutorial on thei(Ve) profile," *J. Neural Eng.*, vol. 13, no. 5, Oct. 2016, Art. no. 052001.

[11] M. M. Maharbiz, W. J. Holtz, S. Sharifzadeh, J. D. Keasling, and R. T. Howe, "A microfabricated electrochemical oxygen generator for high-density cell culture arrays," *J. Microelectromech. Syst.*, vol. 12, no. 5, pp. 590–599, Oct. 2003.

[12] E. L. Cussler, *Diffusion?: Mass Transfer in Fluid Systems*, 3rd ed. Cambridge, U.K.: Cambridge Univ. Press. 2009.

[13] L. Yu and E. Meng, "A dual mode microbubble pressure and flow sensor," in *Proc. IEEE 29th Int. Conf. Micro Electro Mech. Syst. (MEMS)*, Jan. 2016, pp. 325–328.

[14] J. Ortigoza-Diaz *et al.*, "Techniques and considerations in the microfabrication of Parylene C microelectromechanical systems," *Micromachines*, vol. 9, no. 9, p. 422, Sep. 2018.

[15] E. Meng, P.-Y. Li, and Y.-C. Tai, "Plasma removal of Parylene C," *J. Micromech. Microeng.*, vol. 18, no. 4, Apr. 2008, Art. no. 045004.

[16] B. Kim, B. Chen, M. Gupta, and E. Meng, "Formation of three-dimensional Parylene C structures via thermoforming," *J. Micromech. Microeng.*, vol. 24, no. 6, 2014, Art. no. 065003.

[17] C. A. Gutierrez and E. Meng, "Subnanowatt microbubble pressure transducer," *Solid-State Sensors, Actuat. Microsyst. Work.*, pp. 57–60, Jun. 2010.

[18] H. Gensler, R. Sheybani, P.-Y. Li, R. L. Mann, and E. Meng, "An implantable MEMS micropump system for drug delivery in small animals," *Biomed. Microdevices*, vol. 14, no. 3, pp. 483–496, 2012.

[19] R. Sheybani and E. Meng, "High efficiency wireless electrochemical actuators: Design, fabrication and characterization by electrochemical impedance spectroscopy," in *Proc. IEEE 24th Int. Conf. Micro Electro Mech. Syst.*, Jan. 2011, pp. 1233–1236.

[20] S. Saati, R. Lo, P.-Y. Li, E. Meng, R. Varma, and M. S. Humayun, "Mini drug pump for ophthalmic use," *Current Eye Res.*, vol. 35, no. 3, pp. 192–201, Mar. 2010.

[21] D. A. Ateya, A. A. Shah, and S. Z. Hua, "An electrolytically actuated micropump," *Rev. Sci. Instrum.*, vol. 75, no. 4, pp. 915–920, Apr. 2004.

[22] S. Yang and C. Liu, "An electrolysis-bubble-actuated micropump using electrowetting on dielectric (EWOD) for 1XN micro-sample switches," *Transducers*, vol. 2009, pp. 2018–2021, Jun. 2009.

[23] S. Böhm, B. Timmer, W. Olthuis, and P. Bergveld, "A closed-loop controlled electrochemically actuated micro-dosing system," *J. Micromech. Microeng.*, vol. 10, no. 4, pp. 498–504, Dec. 2000.

[24] C. M. Cheng and C. H. Liu, "An electrolysis-bubble-actuated micropump based on the roughness gradient design of hydrophobic surface," *J. Microelectromech. Syst.*, vol. 16, no. 5, pp. 1095–1105, Oct. 2006.

[25] T. M. Lucas and C. K. Harnett, "Control of electrolysis-generated microbubbles for sensor surface passivation," *Appl. Phys. Lett.*, vol. 98, no. 1, Jan. 2011, Art. no. 011915.

[26] J. Sim, D.-S. Kwon, and J. Kim, "Development of pH sensor with enhanced sensitivity using volume of bubbles generated by electrolysis," in *Proc. 27th Transducers Eurosensors, 17th Int. Conf. Solid-State Sensors, Actuat. Microsyst.*, Jun. 2013, pp. 2029–2032.

[27] L. Yu and E. Meng, "A microbubble pressure transducer with bubble nucleation core," in *Proc. IEEE 27th Int. Conf. Micro Electro Mech. Syst. (MEMS)*, Jan. 2014, vol. 122, no. 1, pp. 104–107.

[28] D. A. Ateya, A. A. Shah, and S. Z. Hua, "Impedance-based response of an electrolytic gas bubble to pressure in microfluidic channels," *Sens. Actuators, A, Phys.*, vol. 122, no. 2, pp. 235–241, 2005.

[29] J. Wang, M. Sullivan, and S. Z. Hua, "Electrolytic-bubble-based flow sensor for microfluidic systems," *J. Microelectromech. Syst.*, vol. 16, no. 5, pp. 1087–1094, Oct. 2007.

[30] J. Park, X. He, and C.-S. Kim, "An intelligent dissolved oxygen microsensor system with electrochemically actuated fluidics," in *Proc. IEEE Sensors*, Oct. 2004, pp. 170–173.

[31] C. Pang, Y.-C. Tai, J. W. Burdick, and R. A. Andersen, "Electrolysis-based parylene balloon actuators for movable neural probes," in *Proc. 2nd IEEE Int. Conf. Nano/Micro Eng. Mol. Syst.*, Jan. 2007, pp. 913–916.

[32] D.-S. Meng, Y. Ju, and C.-J. Kim, "A comparative study of electrolysis and boiling for bubble-driven microactuations," in *13rd Int. Conf. Solid-State Sensors, Actuat. Microsyst. Dig. Tech. Papers*, 2005, pp. 1263–1266.
[33] T. Stanczyk, B. Ilic, P. J. Hesketh, and J. G. Boyd, "A microfabricated electrochemical actuator for large displacements," *J. Microelectromech. Syst.*, vol. 9, no. 3, pp. 314–320, Sep. 2000.
[34] L. Hsu, J. Ramunas, J. Gonzalez, J. Santiago, and D. G. Strickland, "Toward an electrolytic micropump actuator design with controlled cyclic bubble growth and recombination," *ECS Trans.*, vol. 35, no. 30, pp. 3–11, Dec. 2011.
[35] C. R. Neagu, J. G. E. Gardeniers, M. Elwenspoek, and J. J. Kelly, "An electrochemical microactuator: Principle and first results," *J. Microelectromech. Syst.*, vol. 5, no. 1, pp. 2–9, Mar. 1996.
[36] P. F. Man, C. H. Mastrangelo, M. A. Burns, and D. T. Burke, "Microfabricated capillarity-driven stop valve and sample injector," in *Proc. IEEE 11st Annu. Int. Workshop Micro Electro Mech. Syst. Invest. Micro Struct., Sensors, Actuat., Mach. Syst. (MEMS)*, Jan. 2005, pp. 107–110.
[37] J. D. Evans and D. Liepmann, "The bubble spring and channel (BSaC) valve: An actuated, bistable, mechanical valve for in-plane fluid control," in *Proc. 10th Int. Conf. Solid-State Sensors Actuators*, 1999, pp. 1122–1125.
[38] W. Satoh, Y. Shimizu, T. Kaneto, and H. Suzuki, "Active on-chip microfluidic transport system based on electrochemical bubble formation and its application to bio/chemical sensing," in *Proc. IEEE Sensors*, Nov. 2005, pp. 167–170.
[39] T. Kurakazu *et al.*, "A selective release method using electrolytically generated bubbles for cell array applications," in *Proc. Int. Solid-State Sensors, Actuat. Microsyst. Conf. (TRANSDUCERS)*, Denver, CO, USA, Jun. 2009, pp. 2362–2365.
[40] R. Goffredo, A. Pecora, L. Maiolo, A. Ferrone, E. Guglielmelli, and D. Accoto, "A swallowable smart pill for local drug delivery," *J. Microelectromech. Syst.*, vol. 25, no. 2, pp. 362–370, Apr. 2016.
[41] S. K. Chung, Y. Zhao, and S. K. Cho, "On-chip creation and elimination of microbubbles for a micro-object manipulator," *J. Micromech. Microeng.*, vol. 18, no. 9, Sep. 2008, Art. no. 095009.

**Eugene Yoon** (Member, IEEE) received the B.S. degree in chemical and biomolecular engineering from Johns Hopkins University in 2015 and the M.S. and Ph.D. degrees in biomedical engineering from the University of Southern California in 2017 and 2021, respectively. He was a 2014 JHU IRES Research Fellow at the Interuniversity Microelectronics Centre, Belgium; presented work at the 2018 National Academy of Inventors Student Showcase, was an NSF INTERN awardee for his work at the National Institute of Standards and Technology in 2020, and was also a Korean American Scientists and Engineers Association Undergraduate and Graduate Scholarship recipient. His research interests include electrochemical bioMEMS sensors, implantable medical devices, and invasive neural interfaces.

**Ellis Meng** (Fellow, IEEE) received the B.S. degree in engineering and applied science and the M.S. and Ph.D. degrees in electrical engineering from the California Institute of Technology (Caltech), Pasadena, in 1997, 1998, and 2003, respectively. Since 2004, she has been with the University of Southern California, Los Angeles, where she was the Viterbi Early Career Chair and then the Department Chair. She is currently the Shelly and Ofer Nemirovsky Chair of Convergent Biosciences and a Professor of biomedical engineering and electrical and computer engineering. She also serves as the Vice Dean for Technology Innovation and Entrepreneurship. Her research interests include bioMEMS, implantable biomedical microdevices, microfluidics, multimodality integrated microsystems, and packaging. She is a fellow of ASME, BMES, AIMBE, and NAI. Her honors include the NSF CAREER Award, the Wallace H. Coulter Foundation Early Career Award, the 2009 TR35 Young Innovator Under 35, the Viterbi Early Career Chair, the ASEE Curtis W. McGraw Research Award, the 2018 IEEE Engineering in Medicine and Biology Society Technical Achievement Award, and the 2019 IEEE Sensors Council Technical Achievement Award.